2023 IEEE International Conference on Robotics and Automation (ICRA 2023)
May 29 - June 2, 2023. London, UK

Trajectory error compensation for optimal control of UMA-2 – a climbing robot executing maintenance operation in harsh environment.

D. Gitardi[1], S. Sabbadini[1] and A. Valente[1]

Abstract — **UMA-2 is a wheeled mobile platform equipped with a vacuum adhesion system, eight actuated joints and four passive ones, designed to climb vertical and curved surfaces. The platform can perform maintenance tasks such as corrosion removal and cleaning with grinding while climbing. The quality of the repairing process is largely affected by grinding process parameters including tool forces, toolpath and the robot trajectory accuracy. The current work introduces a trajectory analysis and adaptation model to control the UMA-2 platform to ensure specific surface quality KPIs and incorporating the effects of robot compliancy. The proposed trajectory analysis has been extensively validated through experimental campaigns representative of maintenance in wind power industry.**

I. INTRODUCTION

The maintenance of surfaces is predominantly performed through manual processes by highly skilled human operators who often work in harsh conditions, such as extreme weather, and are exposed to significant risks to their safety and health [1-4]. During manual execution, the operator applies varying force to the grinding tool and adjusts the pressure and overlaps between single grinding tracks based on coarse visual feedback from the surface quality and fine analysis using a laser-based roughness sensor. This refurbishment of the surface is performed on vertical surfaces, such as wind turbine pillars, whose curvature may vary.

Figure 1. Example of grinding process in harsh working conditions.

Transitioning such a complex task to an automatic robotic platform, presents several challenges, which include: 1) ensuring a grinding trajectory and associated parameters such as depth of cut/grinding force and feed, to target specific quality Key Performance Indicators (KPIs); 2) integrating the tool into a platform that can climb wind turbine pillars made of both metal and concrete surfaces; 3) ensuring that the robot Degrees of Freedom (DoF) and compliancy are as such to accommodate variable surface geometry while accurately following the trajectory required to operate the tool. A multitude of research and commercial robots have been recently developed for climbing applications, typically remotely controlled by operators, using both adhesion and locomotion technologies [5-7]. Vacuum-based robots are typically designed for very low payloads and primarily used for inspection application [8-10]. Robots using magnetic adhesion systems can achieve higher adhesion force and reduce slippage [11-12] but they are limited to ferrous materials. In general, the available solutions are all severely limited by the presence of surface asperities, which could cause the robot to lose contact and the consequent risk to result in critical failures. Specific sensing infrastructures and trajectory control/adaptation models are of instrumental importance for robotic platforms to navigate surfaces [13-19]. Some applications compensate for trajectory errors through linearized tracking error and vision-based control [20-22], but most current approaches and mobile platforms primarily target inspection tasks. Introducing manufacturing technologies, such as grinding and surface brushing, triggers additional challenges for the robot (e.g. payload, battery autonomy, and DoFs) and process optimization. In grinding, key parameters to control include tool contact force, tool rotation speed, and feed rate [23-25], which are optimized with respect to robot compliancy. Examples of process parameters optimization are executed via Proportional-Integral with Velocity feedback (PIV) and Proportional with Feedforward (P + FF) algorithms, [26-27]. The work outlines a trajectory error compensation model for UMA-2, which is an intrinsically compliant structure operating in a kinematically redundant configuration in order to target a grinding tool trajectory that would match KPIs of surface quality. The paper is structured as follows: Sec. II describes UMA-2 robotic platform; Sec. III outlines the trajectory control approach; Sec. IV describes the empirical assessment of the robot trajectory; Sec. V presents the experimental tests and results; Sec. VI summarizes the conclusion and anticipates future works.

II. UMA-2 ROBOTIC PLATFORM

A. Robot architecture

The UMA-2 robot (Fig. 2a) is conceived as a wheel-based mobile platform with a kinematically redundant configuration that combines eight actuated axes, four passive axes, and a flexible vacuum system to climb curved surfaces. The robot infrastructure enables climbing via suction technology but,

* The research has been partially funded by the EU project AVANGARD. Grant agreement no: 869986.

[1] The authors are with the Automation Robots and Machines (ARM) Laboratory at SUPSI – University of Applied Science and Arts of Southern Switzerland, Via la Santa 1, Lugano-Viganello 6962, Switzerland; corresponding author e-mail: diego.gitardi@supsi.ch.

most importantly, the movement across surfaces whose curvature can vary from planar to 4 m diameter. In addition to that, the robot can overcome steps up to 10 mm. The robot presents 950x730x300 mm dimensions with a central area (300x550x160 mm) holding the grinding tool (or any end effector) integrated on a linear axis (Fig. 2b). The robot weights 70 kg and mounts: four-wheel modules (32 kg); six vacuum chambers (8 kg); an aluminium body (5 kg); 24V and 50Ah battery (10 kg); electronics, sensors, control element, and maintenance system (15 kg).

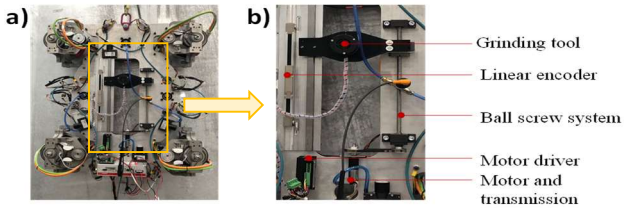

Figure 2. UMA-2 platform prototype (a) and tooling system (b).

The body is conceived as an aluminium 6061 plate whose shape and thickness are designed through an iterative process described in [28]. The four-wheel modules are rigidly connected at a 90° angle to the main body axis. Each wheel module (Fig. 3a) presents two serial actuated joints: DoF1 – driving joint – is enabled by a high torque motor (51 Nm) directly connected to a vulcanized rubber wheel performing its axial rotation; DoF2 – steering joint – consists of a brushless motor (32 Nm) connected to the pulley transmission which actuates the radial wheel rotation. A third passive joint DoF3 – tilting joint – adapts via damping the wheel offset across the surface curvature.

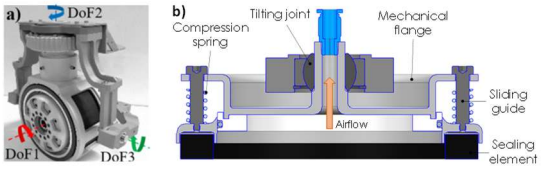

Figure 3. UMA-2 (a) wheel module and (b) vacuum chamber.

Along with the wheel modules, the body hosts a linear axis and a vacuum adhesion system based on a patented concept of adaptable vacuum chambers (Fig. 3b) [29]. Each vacuum chamber consists of a mechanical flange on top of which a tilting joint, rigidly connected to the robot body, ensures the perpendicular position of the chamber with respect to the external surface. The bottom part of the flange integrates four sliding guides with compression springs. The spring-based system connects the vacuum chamber to the body with three main structural advantages: 1) high normal force to the wheels while ensuring the climbing traction; 2) controlled sealing force; 3) robustness to surface asperity without generating high stresses on the robot frame. The embedded tool system (Fig. 2b) consists of a linear axis featuring a maximum stroke of 450 mm and a 2 Nm DC motor connected – through a pulley mechanism (i=2) – to a ball screw driving element rigidly joined with the robot body and a central tool flange.

B. UMA-2 Electric systems and control architecture

The selection of the electronics and auxiliary systems of UMA-2 robot represents a compromise among performances, size, and energy consumption. The control of the joints relies upon Everest XCR EtherCAT DC Servo Drives, an ultra-compact (42x29x23 mm) high-power density (50 A) motor controller. The drives are embedded in the wheels, thus reducing electrical noise and the risks of signal losses. The use of DS402 motion control profile allows sending of real-time target position information from the robot controller to each drive in CSP (Cyclic Synchronous Position) mode and precisely synchronizes the motion of the eight joints of the robot. The developed robot controller includes 2 Intel NUC PCs connected over an internal Gigabit Ethernet network to share the computational loads of motion, navigation, and maintenance tasks. The control architecture and kinematics are implemented in the first NUC PC that controls in real-time the motion of UMA-2. The second NUC hosts the odometry system of the robot elaborating the data coming from proprioceptive and exteroceptive sensors. Both PCs use low-latency patched Ubuntu 18.04 as operating system on the top of which ROS (Robot Operating System) is implemented to manage the data communications between the processes. Along with the control PCs, the robot embeds a battery pack – used to supply 24V to the control PCs, XCR drivers, and the six vacuum pumps – made of 8 LiFePO4 cells serially connected to a Battery Management System. The latter ensures a power source of 24V and 50Ah, 5.5 hours of autonomy, and a total weight of 10 kg (Sec. V).

III. TRAJECTORY CONTROL APPROACH

A. Trajectory optimization model for vertical grinding.

While grinding a patch, the end-effector can execute a number of alternative trajectories. The current work focuses on the easiest zigzag (or raster) trajectory as a baseline. Such a choice is motivated by the need to isolate the contribution of the robot's positioning accuracy from the nominal-actual process trajectory gap (without introducing complexity generated by toolpath strategies). Fig. 4 shows an example of drifting phenomena of uncontrolled robot trajectory (red) with respect to the nominal raster toolpath (black) that results in a poorly grinded patch.

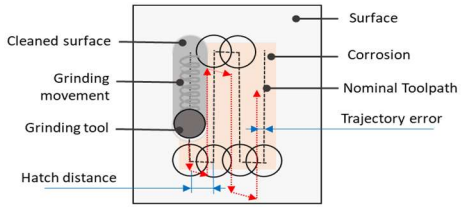

Figure 4. Example of trajectory drifting for grinding process.

The proposed trajectory optimization model (Fig. 5) aims to persistently adapt the robot master trajectory (box 3) in order to match the grinding process strategy (box 2). The nominal repairing path (to be executed at TCP level) results from the set of surface quality KPIs (box 1) – such as surface roughness – and processing strategies (e.g. thick single grinding layer vs multiple thin grinding layers). The TCP trajectory is matched to a robot master trajectory and runs in a redundant manner: the toolpath is discretized into a set of points whose coordinates are mapped – via a custom inverse kinematic model – to the joints' reference frames. The process

dynamics (grinding feed) are then translated into specific motion strategies for the wheels correctly processed by the low-level control (box 4). However, the aforementioned robot master trajectory is only nominal and it is expected to differ from the actual one. Potential trajectory errors are partially associated to the specific status of the surface (generated by corrosion and biological phenomena). A further contribution is to be associated to the robot compliancy that induces positioning accuracy errors. This latter aspect is analysed by running an empirical testing campaign on a quite regular surface (to minimize the surface asperity related contribution). The key idea is to track errors by executing a large set of movements across the vertical direction (contribution of gravity and robot weight on the main robot symmetry axis), the tangent direction (contribution of gravity and robot weight on the second robot symmetry axis) and hybrid combinations of the first two. The measurement method of the error (box 5) between nominal and actual trajectories is described in Sec. IV. Such extensive analysis will lead to the generation of correction coefficients to generate an adapted trajectory (box 6) by integrating them at the control level.

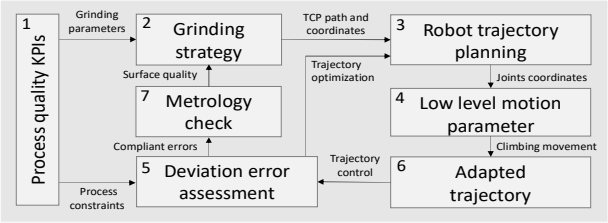

Figure 5. Trajectory control model of UMA-2 robot.

B. *Force equilibrium of vertical grinding task.*

For every discrete point composing the toolpath trajectory, the overall process- and robot-related forces should reach a quasi-static equilibrium (Fig. 6).

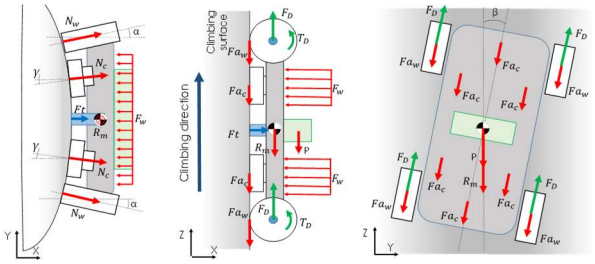

Figure 6. Force scheme of a wheel-based climbing robot.

The variables of the system are: the perpendicular contact force of both the wheel N_w and vacuum elements N_c, the total adhesion force F_w, the tool force F_t, and the driving force F_D. The system of equations across the perpendicular axis Z and longitudinal axis X of the surface is described by (1) and (2).

$$F_D = i \cdot N_w \cdot \mu_r + j \cdot N_c \cdot \mu + \frac{(P+R_m)}{\cos(\beta)} \cdot g \qquad (1)$$

$$j \cdot F_w = F_t + i \cdot N_w \cdot \cos(\alpha) + j \cdot N_c \cdot \cos(\gamma) \qquad (2)$$

Where: i and j represent the number of robot wheels and suction elements (respectively equal to 4 and 6); μ is the friction coefficient of vacuum element; μ_r is the rolling friction coefficient of the wheels; R_m is the robot weight; P is the payload; g the constant of gravity; β is the inclination of robot body; α is the contact angle between the locomotion system and the surface; γ is the contact angle of each vacuum chamber with the surface as function of surface curvature. Equation (3) describes the relation of the vacuum force with the perpendicular reaction forces generated by the wheels and the adhesion elements. As shown in Fig. 7, the reaction force of each vacuum element is equal to the total spring elastic constant K_s multiplied by the displacement Δl of the chamber when the vacuum system is activated.

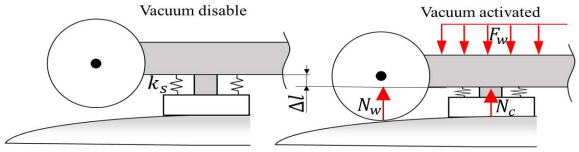

Figure 7. Schematic of force distribution on wheel and vacuum elements.

$$F_w = i \cdot N_w + j \cdot N_c \quad with \quad N_c = K_s \cdot \Delta l \qquad (3)$$

Equation (4) describes the grinding force F_t [30-32] in function of the material removal rate MRR, the feed velocity v_r and the empirical Preston coefficient k_p.

$$F_t = \frac{MRR}{k_p \cdot v_r} \qquad (4)$$

The minimum driving torque T_{req} needed for the wheels to climb a vertical wall can be expressed as the sum of the static torque T_s (force F_D multiplied by the wheel radius r) and the dynamic torque T_d, which represents the torque necessary to accelerate the robot to the nominal velocity. Equation (6) describes the minimum torque, considering the static and dynamic contribution.

$$T_{req} = T_s + T_d \qquad (5)$$

$$T_{req} = r \cdot (F_D + F_{acc}) \qquad (6)$$

Where F_{acc} is the acceleration force of the robot. In order to control the climbing direction, the steering joint is used to achieve the radial rotation of the wheel. The required torque Tr_{req} can be computed as the product of the reaction force N_w between the wheel and the wall multiplied by the friction coefficient μ_w and the wheel width W, as described by (7).

$$Tr_{req} = N_w \cdot \mu_w \cdot 0.5 \cdot W \qquad (7)$$

The listed equations analytically determine the required torque necessary by the joints to perform a grinding task for different position and orientations. For instance, given the UMA-2 configuration (Sec. II) and the variable values listed in Tab. I, a vertical grinding task with 150 mm/s as feed rate require a theoretical adhesion force of 2000 N and nominal axial and radial torques respectively of 37 Nm and 30 Nm.

TABLE I. ASSUMED VARIABLE VALUES FOR MAXIMUM TORQUE AND ADHESION FORCE ESTIMATION.

Variable	μ_w	μ_r	μ	*P [kg]*	K_s *[N/mm]*	Δl*[mm]*
Value	*0.5*	*0.05*	*0.95*	*10*	*5.34*	*15*

IV. EMPIRICAL ASSESSMENT OF THE ROBOT TRAJECTORY

The force equilibrium will lead to a specific set of motion parameters that are computed by assuming that the robotic

platform is not affected by any movement error. In this section, the authors address this very aspect by proposing an empirical approach for measuring trajectory errors. In detail, the robot is commanded to execute a specific set of trajectories that capture the key manoeuvring challenges, and an absolute calibration system measures the robot's position in the Cartesian space (Leica absolute tracker AT960-MR). The campaign is executed on vertical curved steel and flat concrete surfaces without running the grinding process. The empirical study is split into a set of Experimental Tests (ETs).

ET1 – tool contact force – targets the analysis of the robot contact force on the grinding tool. The analysis consists in evaluating the capability of the vacuum system to provide adaptable and controllable adhesion forces as a reaction to the grinding process (i.e. robustly compensating the grinding force). The system is tested both in static conditions (static analysis) and during climbing movements (dynamic analysis) on steel and concrete surfaces.

ET2 – linear climbing movement – analyse the drifting errors of the robot while performing a simple vertical climbing movement. The execution of a linear vertical movement of about 4 m with different climbing velocities (from 140 to 280 mm/s) and incremental payloads (up to 20 kg). The testing campaign allows isolating the effect of the robot compliance on the trajectory accuracy in vertical climbing.

ET3 – grinding cycle – targets the most complex set of tasks where the tool executes multiple overlapped linear grinding operations while following the master nominal trajectory. The drifting errors related to the robot manoeuvre to move the grinding tool from the first vertical grinding operation to the next one. The movement combines the rotation of both driving and steering joints to perform: 1) linear climbing trajectory A; 2) static wheel orientation B; 3) angled climbing trajectory C (Fig. 8).

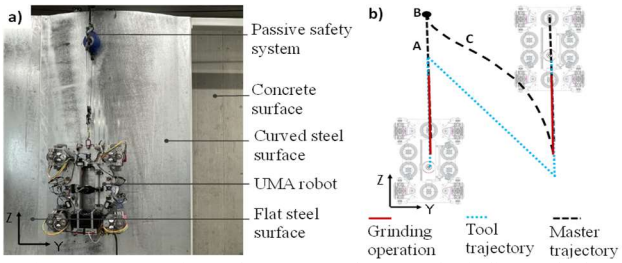

Figure 8. Experimental setup (a) and proposed grinding cycle (b).

Four key KPIs are considered for the empirical assessment. KPI1 regards the perpendicular force generated by the vacuum system as the maximum reaction for the grinding tool. Knowing the minimum vacuum level and the dimension of the chamber, the vacuum adhesion force is computed as the projected area multiplied by the relative vacuum value. The KPI 2 – trajectory deviation error – determines the mismatch between the nominal and actual master trajectories via the absolute tracker. The KPI 3 – joints power consumption – is used to monitor the required power absorbed by the actuators during the climbing movement to appreciate potential slippage phenomena. The power consumption includes the motor current, torque constant, and angular velocity recorded by Everest EXR Drive. Along with trajectory-wise KPIs, an analysis of the robot autonomy – as KPI 4 – is also considered to investigate what is the versatility of the platform to execute multiple alternative processes (some longer than others and therefore more critical with regard to the battery autonomy). A smart shunt resistor is used to record both the state of charge and voltage of the battery pack. The proposed KPIs are all evaluated by sampling signals every 100 ms; the acquired data are successively imported, filtered by Butterworth filter, and processed in Matlab.

V. Experimental Tests and Results

The current section outlines the results associated with the overall approach. In particular, three key aspects have been extensively tested with respect to the use case outlined in the previous section: 1) maximum adhesion force; 2) slippage issues and actuators' power; 3) robot trajectory drifting error.

A. Acceptable grinding force.

The first testing campaign targets the evaluation of the robot's performance enabling the generation of a controlled adhesion force, i.e. the optimal contact force of the tool. The analysis is carried out considering the experimental tests ET1 and the results are evaluated against the KPI1. Fig. 10 shows the adhesion force in static and dynamic conditions for a single vacuum cup controlled with different voltage values on both concrete (Fig. 9a) and steel surfaces (Fig. 9b). Each point of the chart is computed as the mean of 10 repetitions.

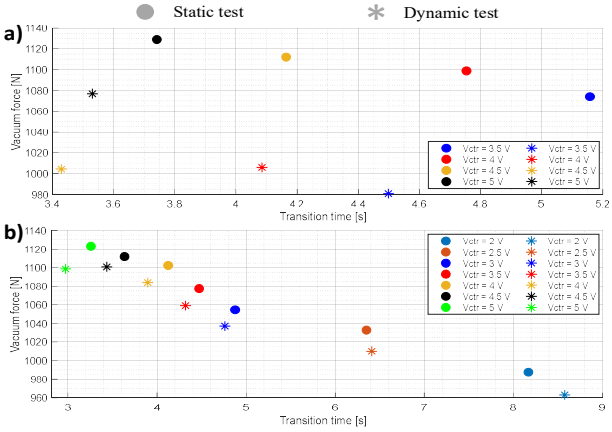

Figure 9. Maximum vacuum force for different supply voltage in static and dynamic conditions: (a) concrete surface; (b) steel surface.

Tab. II lists the transition time required by the vacuum system to evacuate the air inside the chamber (at ambient pressure) and the maximum grinding force applicable to the robot. By assuming a minimum contact force of the wheel necessary to guarantee the climbing movement of the robot – empirically estimated at about 1960 N for concrete and 1930 N for steel – it is possible to cover a quite broad range of grinding forces as listed in Tab. II. UMA-2 platform ensures to handle high grinding forces ranging from about 3850 N to 4600 N thus covering a wide range of grinding applications (e.g. roughing and finishing) characterized by different cutting depth and grinding pressure values.

TABLE II. Acceptable force for grinding process.

		Concrete		*Steel*	
		Acceptable grinding force [N]	*Transition time [s]*	*Acceptable grinding force [N]*	*transition time [s]*
	2	-	-	3852	8.6

Control Voltage (Vc) [V]	***2.5***	-	-	4134	6.4
	3	-	-	4302	4.8
	3.5	3920	4.5	4434	4.3
	4	4070	4.1	4584	3.9
	4.5	4070	3.4	4674	3.4
	5	4520	3.5	4674	3

B. Trajectory behaviour in linear climbing

The movement accuracy of UMA-2 is assessed through an empirical estimation of the trajectory error while performing the vertical climbing movement. The experimental tests are carried out according to the ET2 and the results are analysed against the KPI2 and KPI3 (Sec. IV). This implies computing the trajectory errors along the vertical axis Z, which is the main moving direction (errors along the Y axis are not significant according to a sensitivity analysis). The experiments show that the trajectory of the robot is affected by the payload carried respectively by the platform, the climbing velocity, and the adhesion force generated by the vacuum system. The statistical significance of the error is assessed through a linear regression analysis with a confidence level of 95% and three regressor parameters: driving speed, control voltage of vacuum cup V_c and payload P. The regression model is based on 216 samples (points of the discretized actual master trajectory that are compared to the nominal ones). The validity of the regression is guaranteed by p-values lower than the significant levels together with a high value of R-square as shown in Tab. III.

TABLE III. REGRESSION MODELS OF LINEAR CLIMBING TRAJECTORY.

	Linear regression model equation			
	$y = \text{Intercept} + \beta_v \cdot V + \beta_w \cdot V_c + \beta_p \cdot P$			
Axis	***Estimate coefficient***	***RMSE***	***p-Val***	***R^2***
Z	$\boldsymbol{Intercept = -101.4}$ $\boldsymbol{\beta_v = -6.8 \cdot 10^{-3}}$ $\boldsymbol{\beta_w = 7.03}$ $\beta_p = -1.18$	6.01	$\boldsymbol{\beta_v \rightarrow 0.69}$ $\boldsymbol{\beta_w \rightarrow 4 \cdot 10^{-20}}$ $\beta_p \rightarrow 8 \cdot 10^{-31}$	0.80

The regression model shows that the control voltage and payload are the most significant parameters affecting the movement accuracy along the climbing direction. In detail, for every kg of equipment added to the robot, the trajectory error increases by 1.18 mm while every 1 V increment steps of the control voltage reduce the error of 7.05 mm. Such error can be attributed to two main aspects of the robot: 1) any increment of the payload carried by the robot requires higher torque at the wheel, thus increasing the slippages; 2) a non-uniform distribution of the contact force on the four wheels drives to asymmetric climbing forces and affects the trajectory accuracy. Such behaviour is confirmed by looking at the power consumption of the driving motors. Fig. 10 and 11 show respectively the results of the driving motor power for flat concrete and curved steel surfaces. Each box of Fig. 10a represents the mean driving power consumption and its deviation. The mean power of each test is computed considering the contribution of every single motor and their data distribution (Fig. 10b and Fig. 10c). Fig. 10a outlines an increasing power consumption for every increment of the climbing velocity and almost similar mean power values while increasing the payload. Moreover, the outlier points of some boxes relate to a non-uniform distribution of the power among the four driving joints (Fig. 10b). Such difference in power could be related to a non-uniform distribution of the perpendicular force on the four-wheel modules; it gets worse in case of slippage on the surface as described by peaks and valleys in the single motor power data (Fig. 10c).

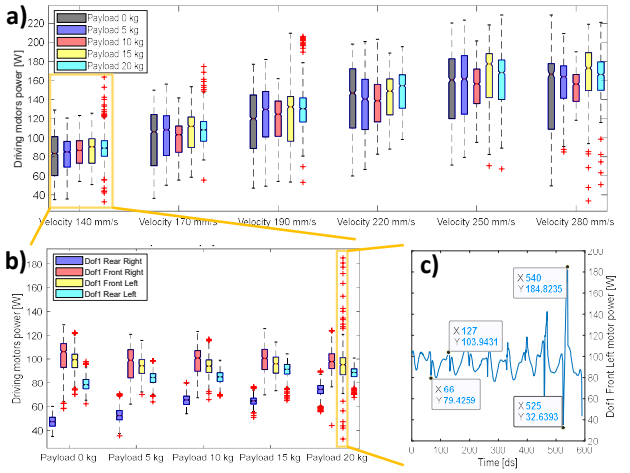

Figure 10. Power consumption while climbing concrete surface: (a) average value, (b) wheel axes contribution; (c) raw power data.

When approaching the steel surfaces, the curved shape allows to achieve a more uniform distribution of the contact force and power on the wheel (Fig. 11b) thus reducing the deviation of the data (Fig. 11a). Moreover, the higher rolling and traction coefficients between the wheel and the steel surface reduces slippage by decreasing the data fluctuations.

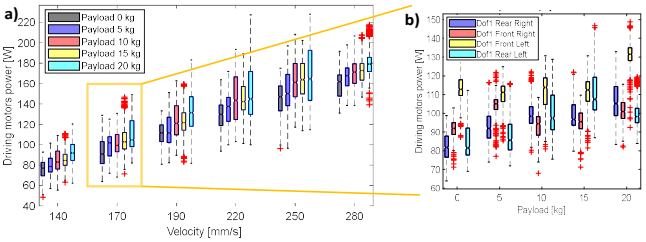

Figure 11. Power consumption while climbing steel surface: (a) average value, (b) wheel axes contribution.

C. UMA-2 compliancy across the grinding cycle

This section presents the trajectory errors of the platform to perform the complex set of tasks presented in the ET3. The experimental results are analysed against the KPI2, KPI3, and KPI4 (Sec. IV). As for the analysis of pure linear movement, also in this case the trajectory errors are modelled through the same regressor parameters (driving speed, control voltage V_c and payload P) with a confidence level of 95%. Considering the nominal trajectory of the robot, the errors are evaluated through two regression models concerning both the Z and Y axes. The validity of the regression models is guaranteed by high R-square values respectively of 0.75 on the Y axis and 0.92 on the Z axis along with lower p-value with respect to significant levels (Tab. IV). Across the Y-axis (p-values of the regressors), the control voltage sent to the vacuum pumps of the robot and payload represent the main parameters influencing the robot master trajectory. Every increment of the control voltage of 1 V, results in a reduction of deviation of about 0.8 mm, while for every kg of payload added to the robot the trajectory error increase by about 0.5 mm. Looking at the regression model of the Z axis, all the regressors are significant with p-values lower than the significant level. Also in this case, the control voltage represents the most affecting parameter: each increment of 90 N reduces errors of 11.5 mm.

TABLE IV. REGRESSION MODELS OF GRINDING TRAJECTORY.

	Linear regression model equation			
	$y = \text{Intercept} + \beta_v \cdot V + \beta_w \cdot V_c + \beta_p \cdot P$			
Axis	***Estimate coefficient***	***RMSE***	***p-Val***	***R^2***
Y	$\boldsymbol{Intercept = -19}$ $\boldsymbol{\beta_v = -2.2 \cdot 10^{-2}}$ $\boldsymbol{\beta_w = 0.77}$ $\beta_p = -0.555$	6.21	$\boldsymbol{\beta_v \rightarrow 0.18}$ $\boldsymbol{\beta_w \rightarrow 5.9 \cdot 10^{-4}}$ $\beta_p \rightarrow 5.2 \cdot 10^{-2}$	0.65
Z	$\boldsymbol{Intercept = -190}$ $\boldsymbol{\beta_v = 0.12}$ $\boldsymbol{\beta_w = 11.5}$ $\beta_p = -2.83$	7.62	$\boldsymbol{\beta_v \rightarrow 2.2 \cdot 10^{-13}}$ $\boldsymbol{\beta_w \rightarrow 7.9 \cdot 10^{-54}}$ $\boldsymbol{\beta_p \rightarrow 1.8 \cdot 10^{-108}}$	0.92

The estimated coefficients and significant regressors are implemented in a feedforward trajectory control and optimization, which corrects the joint's target positions Θ with the error $\hat{\varepsilon}$ predicted by the model computed considering the time-dependent robot operating set-up, driving motor's velocity feedback, and control voltage of vacuum pumps.

$$\hat{\Theta}(k \cdot T_s) = \Theta(k \cdot T_s) - \hat{\varepsilon}(k \cdot T_s) \quad (8)$$

With: T_s is the time step of trajectory discretization, k is the time index, and $\hat{\Theta}$ is the corrected target position. Fig.12a shows a sequence of three successive vertical movements (ET2) and the consequent cumulating error measured with tracker AT960-MR. Fig.12b shows the compensation of the final error (95%) resulting from the feedforward controller.

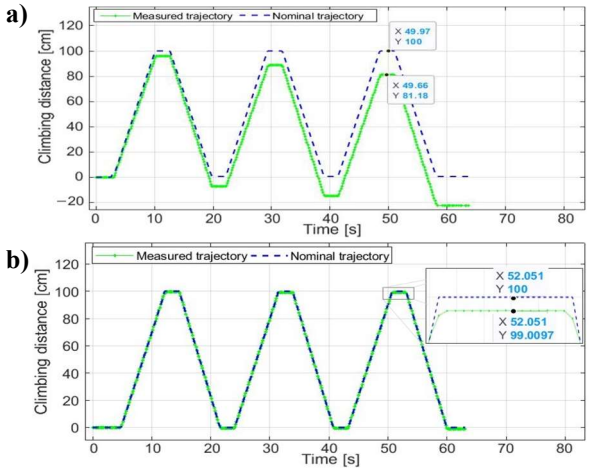

Figure 12. Trajectory accuracy without (a) and with (b) feedforward control.

Concerning the steering joints, precise power consumption values (Fig. 13) represent an accurate wheel orientation, slippage-free.

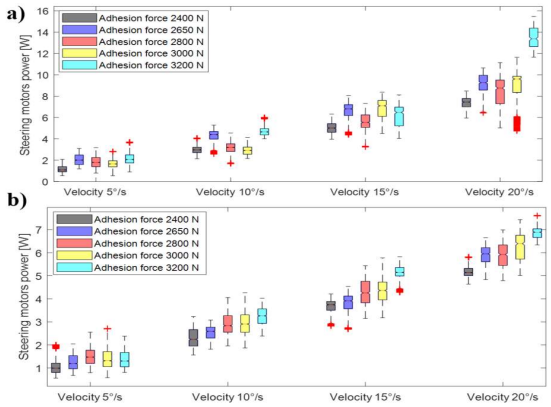

Figure 13. Power consumption of steering motor on concrete surface (a) and on steel surface (b).

During the cycle tests, three payloads (0, 10, and 20 kg) and four driving velocities (70, 140, 210, and 280 mm/s) are used to experimentally measure the maximum autonomy of the robot (KPI4). Each climbing cycle is repeated until the complete discharge of the battery to exactly estimate the robot's autonomy (Fig. 14). Fig. 15 describes the effect of climbing velocity and payload on the autonomy of the platform. Higher climbing velocities and payloads reduce the autonomy of the platform from 5.5 h (0 kg payload and 70 mm/s) to 2.8 h (280 mm/s with 20 kg).

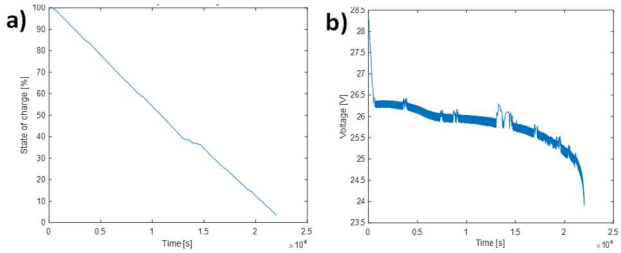

Figure 14. Characteristic curve of LiFoPO4 battery pack for a complete discharge: (a) State of charge; (b) battery voltage.

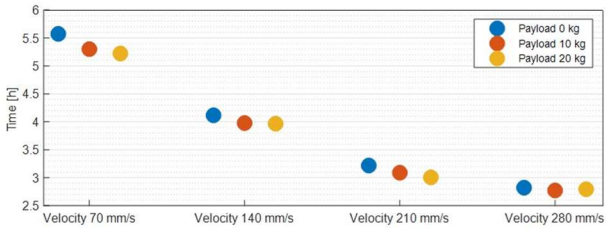

Figure 15. UMA-2 autonomy for different climbing velocity and payload.

VI. CONCLUSION AND FUTURE WORK

The paper presents an application for mobile platforms, which integrates manufacturing technologies, particularly grinding, with the most popular tasks wind towers maintenance and servicing. The study focused on isolating and adapting the positioning error caused by compliancy, implementing feedforward control for trajectory optimization, and considering the surface and process KPIs. Experimental tests were conducted to validate the UMA-2 robot's ability to climb vertical and curved metal and concrete surfaces while delivering high perpendicular force, supporting 20 kg of payload, and thereby assisting human operators in executing extremely hazardous tasks while relieving them of cognitive and physical strain.

Future works will concentrate extensively on grinding process strategies, while integrating the tool wear compensation mechanism and related trajectory adaptation. Additional efforts will focus on validating the model's robustness against environmental phenomena that can cause wet, icy, and hot surfaces. Finally, a shared localization model will be designed for maintenance planning in wind power.

REFERENCES

[1] B. Busch, G. Cotugno, M. Khoramshahi, G. Skaltsas, D. Turchi, L. Urbano, M. Wächter, Y. Zhou, T. Asfour, G. Deacon and D. Russell, "Evaluation of an Industrial Robotic Assistant in an Ecological Environment," 2019 28th IEEE International Conference on Robot and Human Interactive Communication (RO-MAN), pp. 1-8, 2019.

[2] T. Yoshiike, M. Kuroda, R. Ujino, H. Kaneko, H. Higuchi, S. Iwasaki, Y. Kanemoto, M. Asatani and T. Koshiishi, "Development of experimental legged robot for inspection and disaster response in plants," 2017 IEEE/RSJ International Conference on Intelligent Robots and Systems (IROS), 2017.

[3] E. Alati, L. Mauro, V. Ntouskos and F. Pirri, "Anticipating Next Goal for Robot Plan Prediction," Intelligent Systems and Applications. IntelliSys 2019. Advances in Intelligent Systems and Computing, vol 1037, pp. 792-809, 2020.

[4] V. Ntouskos, M. Sanzari, E. Alati, L. Freda and F. Pirri, "Visual search and recognition for robot task execution and monitoring," in Applications of Intelligent Systems, Vol. 310, pp. 94-109, 2018.

[5] D. Gitardi, M. Giardini and A. Valente, "Autonomous robotic platform for inspection and repairing operations in harsh environments," International Journal of Computer Integrated Manufacturing, Vol. 34:6, pp. 666-684, 2021.

[6] H. Eto and H. H. Asada, "Development of a Wheeled Wall-Climbing Robot with a Shape-Adaptive Magnetic Adhesion Mechanism," 2020 IEEE International Conference on Robotics and Automation (ICRA), pp. 9329-9335, 2020.

[7] D. Ge, Y. Tang, S. Ma, T. Matsuno and C. Ren, "A pressing attachment approach for a wall-climbing robot utilizing passive suction cups," in Robotics, 9.2: 26, 2020.

[8] Q. Zhou and X. Li, "Experimental investigation on climbing robot using rotation-flow adsorption unit," in Robotics and Autonomous Systems, Vol. 105, pp. 112-120, 2018.

[9] A. Shujah, H. Habib, S. Shaikh, A. R. Ishfaq, H. Tahir and J. Iqbal, "Design and Implementation of Semi-Autonomous Wall Climbing Robot Using Vacuum Suction Adhesion," 2019 IEEE 17th World Symposium on Applied Machine Intelligence and Informatics (SAMI), pp. 275-280, 2019.

[10] N. K. Nguyen, C. C. Nguyen and N. T. Bui, "A Study of Wall-Climbing Robot for Cleaning Silo Using Vacuum Principle," in International Journal of Mechanical Engineering and Robotics Research, Vol. 10(7), pp. 368-373, 2021

[11] J. Hu, X. Han, Y. Tao and S. Feng, "A magnetic crawler wall-climbing robot with capacity of high payload on the convex surface," in Robotics and Autonomous Systems, Vol. 148, 103907, 2022.

[12] O. Kermorgant, "A magnetic climbing robot to perform autonomous welding in the shipbuilding industry," in Robotics and Computer-Integrated Manufacturing, Vol. 53, pp. 178-186, 2018.

[13] W. Xu, J. Wei, J. M. Dolan, H. Zhao and H. Zha, "A real-time motion planner with trajectory optimization for autonomous vehicles," 2012 IEEE International Conference on Robotics and Automation, pp. 2061-2067, 2012.

[14] M. McNaughton, C. Urmson, J. M. Dolan and J. -W. Lee, "Motion planning for autonomous driving with a conformal spatiotemporal lattice," 2011 IEEE International Conference on Robotics and Automation (ICRA), pp. 4889-4895, 2011.

[15] M. McNaughton, "Parallel algorithms for real-time motion planning," Carnegie Mellon University, 2011.

[16] A. Kelly and B. Nagy, "Reactive nonholonomic trajectory generation via parametric optimal control," in The International Journal of Robotics Research, Vol. 22(7-8), pp. 583-601, 2003.

[17] B. Nagy and A. Kelly, "Trajectory generation for car-like robots using cubic curvature polynomials," in Field and Service Robots, Vol. 11, pp. 479-490, 2001.

[18] D. Dolgov, S. Thrun, M. Montemerlo and J. Diebel, "Practical search techniques in path planning for autonomous driving," Ann Arbor, 1001(48105), pp. 18-80, 2008.

[19] M. Zucker, J. Andrew Bagnell, C. G. Atkeson and J. Kuffner, "An optimization approach to rough terrain locomotion," 2010 IEEE International Conference on Robotics and Automation (ICRA), pp. 3589-3595, 2010.

[20] G. Klančar and I. Škrjanc, "Tracking-error model-based predictive control for mobile robots in real time," in Robotics and autonomous systems, Vol. 55(6), pp. 460-469, 2007.

[21] H. Mirzaeinejad and A. Shafei, "Modeling and trajectory tracking control of a two-wheeled mobile robot: Gibbs–Appell and prediction-based approaches," in Robotica, Vol. 36(10), pp. 1551-1570, 2018.

[22] Z. Li, C. Yang, C. -Y. Su, J. Deng and W. Zhang, "Vision-Based Model Predictive Control for Steering of a Nonholonomic Mobile Robot," in IEEE Transactions on Control Systems Technology, vol. 24, no. 2, pp. 553-564, 2016.

[23] S. N. Padmanabhan, Z. Halil, Y. Sun, T. T. Vu, S. H. Yeo and A. Wee, "Experimental investigation of Robotic Surface Finishing Using Abrasive Disc," in International Journal of Materials, Mechanics and Manufacturing, Vol. 6, pp. 127-130, 2018.

[24] Y. Wen, J. Hu and P. R. Pagilla, "A Novel Robotic System for Finishing of Freeform Surfaces," 2019 International Conference on Robotics and Automation (ICRA), pp. 5571-5577, 2019.

[25] Y. Dong, T. Ren, K. Hu, D. Wu and K. Chen, "Contact force detection and control for robotic polishing based on joint torque sensors," in The International Journal of Advanced Manufacturing Technology, Vol. 107(5), pp. 2745-2756, 2020.

[26] R. Pérez-Ubeda, R. Zotovic-Stanisic and S. C. Gutiérrez, "Force control improvement in collaborative robots through theory analysis and experimental endorsement," in Applied Sciences, Vol. 10(12), pp. 4329, 2020.

[27] R. P. Ubeda, S. C. Gutiérrez Rubert, R. Z. Stanisic and Á. Perles Ivars, "Behavioural study of the force control loop used in a collaborative robot for sanding materials," in Materials, Vol. 14(1), pp. 67, 2020.

[28] D. Gitardi, S. Sabbadini, A. Valente, "UMA Universal Maintenance Automata – an adaptable robotic platform designed to run maintenance operations in harsh environment," in Procedia CIRP, Vol. 107, pp. 1473-1478, , 2022.

[29] D. Gitardi, S. Sabbadini, A. Valente, "Vacuum cap for robotic system, robotic system comprising the vacuum cup, and method for providing tight hold of the vacuum cup on uneven surfaces," EU patent EP21174904.9, May 20, 2021.

[30] A. Guiot, S. Pattofatto, C. Tournier and L. Mathieu, "Modeling of a polishing tool to simulate material removal," in Advanced Materials Research, Vol. 223, pp. 754-763, 2011.

[31] M. Xiao, Y. Ding, Z. Fang and G. Yang, "Contact force modeling and analysis for robotic tilted-disc polishing of freeform workpieces," in Precision Engineering, Vol. 66, pp. 188-200, 2020.

[32] Y. Kakinuma, S. Ogawa and K. Koto, "Robot polishing control with an active end effector based on macro-micro mechanism and the extended Preston's law," in CIRP Annals, Vol. 71, 2022.